Flow (2022), **2** E9
doi:10.1017/flo.2022.2

FLOW CAMBRIDGE UNIVERSITY PRESS

RESEARCH ARTICLE

Time-averaged velocity and scalar fields of the flow over and around a group of cylinders: a model experiment for canopy flows

D. D. Wangsawijaya[1,*], C. Nicolai[1] and B. Ganapathisubramani[1]

[1]Aerodynamics and Fluid Mechanics Research Group, Faculty of Engineering and Physical Sciences, University of Southampton, SO17 1BJ, UK
*Corresponding author. E-mail: D.D.Wangsawijaya@soton.ac.uk

Received: 26 October 2021; **Revised:** 5 February 2022; **Accepted:** 17 February 2022

Keywords: Mixing and dispersion; Wakes; Turbulent boundary layers; Urban fluid dynamics; Mixing enhancement; Turbulence control

Abstract

We conduct a well-controlled model experiment for a wide variety of canopy flows. Examples of these include engineering flows such as wind flow, dispersion of scalars through and over urban areas, and the convective heat transfer in many heat exchangers, as well as natural canopies such as flows through terrestrial or aquatic vegetation. We aim to shed the light on fundamental flow and transport phenomena common to these applications. Specifically, the characteristics of mean flow and scalar concentration characteristics of a turbulent boundary layer flow impinging on a canopy, which comprises a cluster of tall obstacles (this can also be interpreted as a porous obstruction). The cluster is created with a group of cylinders of diameter d and height h arranged in a circular patch of diameter D. The solidity of the patch/obstruction is defined by ϕ (the total planar area covered by cylinders), which is systematically varied ($0.098 \leq \phi \leq 1$) by increasing the number of cylinders in a patch (N_c). A point source is placed at ground level upstream of the patch and its transport over and around the patch is examined. Time-averaged velocity and scalar fields, obtained from simultaneous planar particle image velocimetry-planar laser-induced fluorescence (PIV-PLIF) measurements, reveal that the characteristics of wake and flow above porous patches are heavily influenced by ϕ. In particular, we observe that the horizontal and vertical extent of the wake and scalar concentration downstream of the patches decreases and increases with ϕ, respectively. Here, the recirculation bubble is shifted closer to the trailing edge (TE) of the patches as ϕ increases, limiting the flow from convecting downstream, decreasing the scalar concentration and virtually 'extending' the patch in the streamwise direction. As the bubble forms in the TE, vertical bleeding increases and hence the concentration increases above the patch where the cylinders appear to 'extend' vertically towards the freestream.

Impact Statement

Canopy flow covers extensive phenomena encountered in both nature and engineering applications. The characteristics of canopies (also referred to as porous obstructions) is known to affect the mixing, momentum and scalar (e.g. mass and heat) exchange processes in the flow. Examples include flow over and around urban areas, wind/tidal farms, patches of roughness in ship hulls, in-line heat-exchangers among various others. In almost all these applications, the patch of obstacles/roughness is typically characterised by its geometric properties, such as solidity (frontal and plan) or porosity, and it is important to understand the

flow/scalar characteristics as well as transport processes for varied geometric parameters. For instance, an urban canopy with a given distribution of buildings and a pollutant source at ground level could result in different wake/dispersion characteristics depending on the frontal or plan solidity of distribution. This study attempts to carry out simplified experiments that will enable us to understand the intricacies of scalar-momentum transport over and around such canopies and allow us to build useful models for engineering design and/or prediction for engineering and environmental flows.

1. Introduction

Canopy flow refers to a scenario where a boundary layer develops over and around a porous surface/obstruction. Examples of such a phenomenon abound in both nature and engineering applications, including but not limited to flows past aquatic and terrestrial vegetations, atmospheric boundary layers developing over forests, clusters of tall buildings in cities, and wind/tidal farms, which consist of arrays of wind/tidal turbines. These obstructions are known to affect the scalar, momentum and energy transport process in the flow within the canopy and downstream of the canopies. Aquatic vegetation, for example, provides shielding (Kemp, Harper, & Crosa, 2000), affects the sediment formation and erosion (De Langre, 2008; Nepf, 2012a, 2012b; Tinoco & Coco, 2016), and also carbon sequestration in coastal ecosystems (Lei & Nepf, 2021). Urban and vegetation canopies induce coherent, multi-scale turbulent motions in the atmospheric boundary layer (Huang, Cassiani, & Albertson, 2009a, 2009b, 2011; Kanda, 2006; Katul, Kuhn, Schieldge, & Hsieh, 1997; Li & Bou-Zeid, 2011), which governs flow mixing, momentum, heat and mass exchange within the layer (Finnigan, 2000; Poggi, Porporato, Ridolfi, Albertson & Katul, 2004; Raupach & Thom, 1981), including pollutants and other chemical compounds (Aristodemou et al., 2018; Poggi, Katul, & Albertson, 2006). While the configuration and tuning of turbines in wind/tidal farms are vital in maximising power output (Myers & Bahaj, 2012; Vennell, 2011), they may also alter the meteorological pattern and ecosystem of the installation sites. For example, the installation of wind turbines has been shown to affect the temperature distribution and humidity of the surrounding air (Baidya Roy, Pacala, & Walko, 2004; Rajewski, Takle, Prueger, & Doorenbos, 2016), while wakes generated by tidal turbines can potentially modify the sedimentation process and bacterial population in estuarine waters (Ahmadian, Falconer, & Bockelmann-Evans, 2012). Considering its extensive industrial applications and environmental impacts, understanding the transport mechanism of the flow surrounding porous obstructions is, therefore, essential.

Previous studies on porous obstructions (such as the examples given above) have typically involved some simplifications from real-life conditions. The obstruction may be simplified as an array of cylinders mounted on an isolated patch with an incoming flow upstream of the cylinders (illustrated in figure 1). Numerical simulations and experiments have been conducted on the flow surrounding such a cylindrical array (Ball, Stansby, & Allison, 1996; Chang & Constantinescu, 2015; Chang, Constantinescu, & Tsai, 2017; Chen, Ortiz, Zong, & Nepf, 2012; Nepf, 1999; Nepf, Mugnier, & Zavistoski, 1997; Nicolle & Eames, 2011; Rominger & Nepf, 2011; Tanino & Nepf, 2008; White & Nepf, 2003; Zong & Nepf, 2012), where the cylinders are as tall as, or protruding from, a free surface, as commonly observed in emergent aquatic vegetation. Here, the flow is dominated by a Kármán vortex street in the wall-normal axis trailing behind the cylinders and thus can be considered two-dimensional (2-D) (Nicolai, Taddei, Manes, & Ganapathisubramani, 2020; Taddei, Manes, & Ganapathisubramani, 2016). A more general approach is to fully submerge the cylinders in the flow such that the height $h \ll \delta_{bl}$, where δ_{bl} is the incoming boundary-layer thickness (figure 1*b*). Studies have been conducted for cylinders attached to a bottom wall (as in figure 1*b*, see also Chen, Jiang, & Nepf, 2013; Nicolai et al., 2020; Taddei et al., 2016) and/or suspended from a free surface (Plew, 2011; Tseung, Kikkert, & Plew, 2016; Zhou & Venayagamoorthy, 2019). In either case, the patch is considered as three-dimensional (3-D), as flow mixing occurs on the sides of, downstream of and above the body. Taddei et al. (2016), Zhou and Venayagamoorthy (2019), Nicolai et al. (2020) have identified three mechanisms in which the flow may escape ('bleed') from a fully submerged porous obstruction: (i) the lateral bleeding from the interior

https://doi.org/10.1017/flo.2022.2 Published online by Cambridge University Press

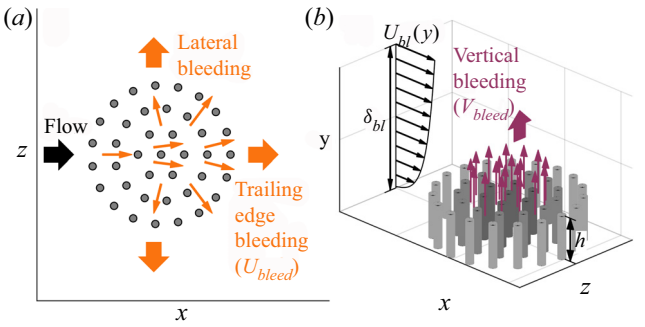

Figure 1. *Illustrations of (a) lateral and trailing edge bleeding, and (b) vertical bleeding of cylindrical arrays on a circular patch. Here, U_{bl} is the incoming boundary-layer velocity, whose thickness is δ_{bl}, and h is the height of the cylinders.*

of the patch to the sides (spanwise direction, see figure 1*a*); (ii) the trailing edge (TE) bleeding, which is responsible in the formation of wake downstream of the body (figure 1*a*); and (iii) the vertical bleeding, in which the flow escapes from the interior to the top surface of the patch and towards the free stream (figure 1*b*).

It has been reported that the solidity of a porous obstruction is a critical parameter in determining drag (Chang et al., 2017; Nepf, 1999; Taddei et al., 2016; Zhou & Venayagamoorthy, 2019), the structure of wake formed by the obstruction (Ball et al., 1996; Chang & Constantinescu, 2015; Chang et al., 2017; Chen et al., 2012; Nicolai et al., 2020; Nicolle & Eames, 2011; Zhou & Venayagamoorthy, 2019; Zong & Nepf, 2012), scalar dispersion (Nepf et al., 1997; Tanino & Nepf, 2008; White & Nepf, 2003) and sediment disposition (Chang & Constantinescu, 2015; Chen et al., 2012). For the cylindrical array shown in figure 1, the solidity is measured in terms of the planar area covered by cylinders per total surface, $\phi \equiv N_c(d/D)^2$ (also commonly referred to as the solid volume fraction), where N_c is the number of cylinders in a circular patch, D is the diameter of the circular patch and d is the diameter of the cylinder (see figure 2*a*,*d* for graphical descriptions of D and d). It has been observed by Nicolle and Eames (2011), Taddei et al. (2016), Zhou and Venayagamoorthy (2019) that the total drag of the patch C_D increases with the increasing ϕ then drops for a solid obstruction ($\phi = 1$, figure 2*d*). Higher patch solidity also yields shorter and taller wake (in streamwise and wall-normal direction, respectively, see Nicolai et al., 2020) in the trailing edge, and increases both lateral and vertical bleeding (Zhou and Venayagamoorthy (2019), see also figure 1). Further, it has been reported by Nicolle and Eames (2011) that at low ϕ($\phi < 0.05$), each cylinder in an array behaves as a single obstruction and as the solidity increases to $\phi > 0.15$, the cylindrical array behaves closer to a solid obstruction whose size is equal to that of the patch ($\phi = 1$, figure 2*d*). Within the range of moderate solidity ($0.05 \leq \phi \leq 0.15$), suppression of vortex street formation downstream of 2-D porous patches has been observed. In its place is a steady wake (constant velocity) region, which is a consequence of flow bleeding. Zong and Nepf (2012) and Chen et al. (2012) showed that the streamwise length of this steady wake region scales on C_DaD, where a is the frontal area per unit volume $a \equiv N_c d/(0.25\pi D^2)$. Similarly, scaling by C_Dab and C_Dah have also been observed by Rominger and Nepf (2011) for a square patch and by Chen et al. (2013) for a fully submerged patch, respectively, where b is the half-width of the patch.

Although the characteristics of the wake and drag of a porous obstruction shown in figure 1 have been discussed in detail for both 2-D and 3-D patches, an element that is still missing from these analyses is the intricacy between bleeding and scalar transport in 3-D porous patches. So far, discussions about scalar transport are limited to lateral and longitudinal dispersion in 2-D patches (Tanino & Nepf, 2008; White & Nepf, 2003), sediment deposition (Chen et al., 2012; Tinoco & Coco, 2016), qualitative flow visualisation using dye injection (Ball et al., 1996; Rominger & Nepf, 2011; Zong & Nepf, 2012), and non-simultaneous velocity and scalar measurements due to limitations of the experimental facilities

https://doi.org/10.1017/flo.2022.2 Published online by Cambridge University Press

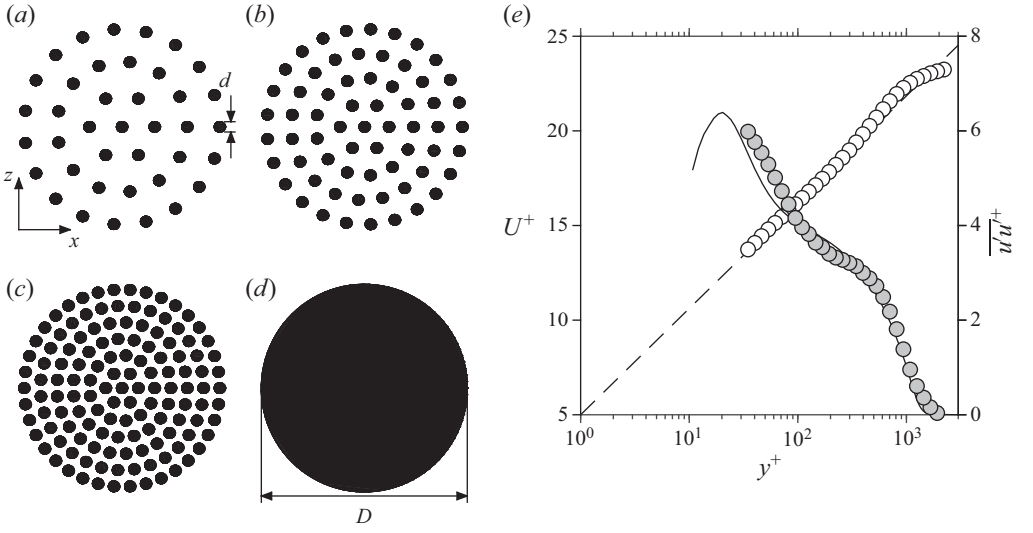

Figure 2. *Illustration of cylinder array test cases: (a) C39; (b) C64; (c) C133; and (d) the solid case (CS) in the x–z plane (top view), d is cylinder diameter and D is the circular patch diameter. (e) Mean streamwise velocity U^+ (∘) and variance of velocity fluctuation $\overline{u'u'}^+$ (•, light grey) of the smooth-wall turbulent boundary-layer (TBL) case as functions of wall-normal location y^+ at $Re_\theta \approx 3000$, where θ is the momentum thickness. Dashed line is $1/(0.41)\log y^+ + 5.0$, solid line is the DNS results of Sillero et al. (2014) at $Re_\theta = 4000$, filtered according to the spatial resolution of the PIV measurements (Lee et al., 2016). Data are downsampled for clarity.*

(Nepf, 1999; Tanino & Nepf, 2008). Here, a 3-D porous patch serves as a more realistic model of urban landscapes, vegetation canopies and wind farms, which are typically subsumed within the atmospheric boundary layer. Inclusion of scalar measurements (in addition to the velocity components) has many potential benefits, for example, in air pollution studies, where one might consider cluster of densely populated urban landscape as a porous obstruction and the pollutant as scalar, or in studies about sediment disposition in ocean beds.

In this study, we aim to address the following question: given a point source of scalar located at the ground level just upstream of 3-D porous patches, what are the flow and scalar characteristics in the wake and above the patches for various solidities? To answer this question, we conduct a parametric study of turbulent boundary layers impinging on an array of cylinders mounted on a circular patch (see figure 1). A point source upstream of the patch is created by releasing a passive fluorescent dye. The solidity ϕ is varied by systematically increasing the number of cylinders in the patch, such that $0.098 \leq \phi \leq 1$. This covers both the medium and high solidity range described by Nicolle and Eames (2011). The axis system (x, y, z) corresponds to the streamwise, wall-normal and spanwise direction, respectively. Simultaneous planar particle image velocimetry-planar laser-induced fluorescence (PIV-PLIF) measurements in the x–y plane provide the instantaneous streamwise–wall-normal velocity components u and v, respectively, and the scalar concentration field c, which can be decomposed further into their time-average and fluctuation about the mean

$$u(x, y, t) = U(x, y) + u'(x, y, t); \quad v = V + v'; \quad c = C + c'. \tag{1.1a–c}$$

It should be noted that due to the choice of the measurement plane, discussion about flow bleeding in the current study is limited only to the trailing edge and vertical bleeding (figure 1).

https://doi.org/10.1017/flo.2022.2 Published online by Cambridge University Press

Table 1. *List of cylinder array test cases. Here, N_c is the number of cylinders in a patch, d and D are the diameters of the cylinders and the patch, respectively, h is the height of the cylinders, ϕ is patch solidity, and a is the frontal area per unit volume. The 'PIV' and 'PLIF' columns show the availability of PIV and PLIF images of each test case. The last three columns show the availability of those images in each field of view (FOV).*

Cases	N_c	ϕ	aD	PIV	PLIF	FOV 1	FOV 2	FOV 3
C39	39	0.098	2.483	✓	✓	✓	✓	✓
C64	64	0.160	4.074	✓	✓	✓	✓	✓
C133	133	0.333	8.467	✓	✓	✓	✓	✓
CS	1	1	1.273	✓	✓	✓	✓	✗
TBL	—	—	—	✓	✗	✓	✓	✗

2. Experimental set-up

2.1. Test cases

Experiments are carried out in the closed loop water flume at the University of Southampton. The test section has the size of 6250 mm × 1200 mm (length × width). In all measurements, the water level is kept constant at 600 ± 1 mm and the free stream velocity is set to $U_\infty \approx 0.45$ ms^{-1}. The free stream turbulence level is ∼1 %.

A circular patch with a diameter (D) of 100 mm is mounted on the floor of the tunnel at 5500 mm downstream of the test section entrance, which corresponds to the patch Reynolds number $Re_D \equiv U_\infty D/\nu \approx 4.5 \times 10^4$, where $\nu = 1.0035 \times 10^{-6}$ m^2 s^{-1} is the kinematic viscosity of water at 20 °C. The patch constitutes an array of rigid cylinders, each has the diameter of $d = 5$ mm and height $h = 30$ mm (figures 1*b* and 2*a*,*d*), which correspond to $d/D = 0.05$ and $h/D = 0.3$. The cylinders are arranged along concentric, evenly spaced circles whose axis is at the centre of the circular patch, such that the distance between two consecutive cylinders is constant within the patch (see figure 2*a–c*). The solidity of the patch is parametrically varied by gradually increasing the number of cylinders N_c while keeping D and d constant. Table 1 and figure 2(*a–c*) show three different circular patches: C39, C64, C133, which correspond to $N_c = 39$, 64, 133, which cover a range of patch densities of $0.1 \lesssim \phi \lesssim 0.33 (2.5 \lesssim aD \lesssim 8.5)$. A solid obstruction case, i.e. a cylinder covering the entire circular patch (such that $N_c = 1$ and $\phi = 1$), is included in addition to the porous cases as case 'CS' in table 1 and figure 2(*d*). The solid cylinder in case CS has an equal height h to the cylinder arrays in other test cases.

2.2. Validation with smooth-wall turbulent boundary layer

A smooth-wall turbulent boundary layer (TBL) case is first tested to validate PIV measurements in the present study. The measurement is conducted in the same test section as other test cases by removing the circular patch. This flow has the Reynolds number (based on momentum thickness θ) of $Re_\theta \equiv \theta U_\infty/\nu \approx 3000$ and friction Reynolds number $Re_\tau \equiv \delta_{bl} U_{\tau bl}/\nu \approx 1500$, where $\delta_{bl} = 82 \pm 3$ % mm is the 99 % boundary-layer thickness, $U_{\tau bl} \equiv \sqrt{\tau_0/\rho} = 0.019 \pm 2$ % ms^{-1} is the friction velocity for this case, τ_0 is the wall shear stress and $\rho = 998.12$ kg m^{-3} is the density of water at 20 °C. Figure 2(*e*) shows the profiles of mean streamwise velocity $U^+ \equiv U/U_{\tau bl}$ and the variance of velocity fluctuations $\overline{u'u'}^+ \equiv \overline{u'u'}/U_{\tau s}^2$ as functions of wall-normal location $y^+ \equiv yU_{\tau s}/\nu$, where subscript '+' denotes viscous scaling and the viscous length scale is $\nu/U_{\tau s} = 0.053$ mm. The logarithmic region of the mean velocity collapses to the line $1/\kappa \log y^+ + A$, where $\kappa = 0.41$ is the von Kármán constant and $A = 5.0$ is the log-law shift (Schlichting & Gersten, 2017). The variance $\overline{u'u'}$ is in good agreement with that obtained from the direct numerical simulation (DNS) of Sillero, Jiménez, and Moser (2014) at $Re_\theta = 4000$. Note that the DNS results presented in figure 2(*e*) are filtered according to the spatial resolution of the

https://doi.org/10.1017/flo.2022.2 Published online by Cambridge University Press

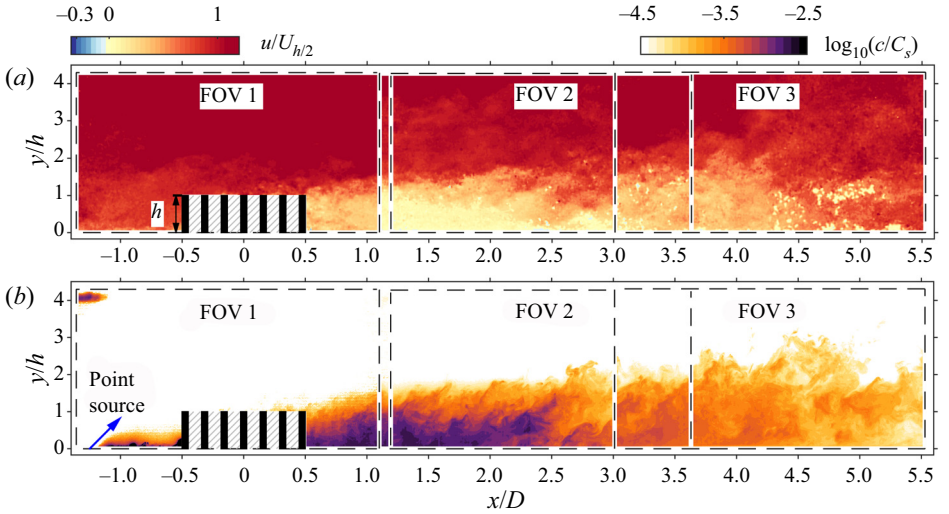

Figure 3. *Contours of instantaneous (a) streamwise velocity $u/U_{h/2}$ and (b) scalar concentration c/C_s (in logarithmic scale) of case C39, obtained from (a) PIV and (b) PLIF measurements, where $U_{h/2}$ is the incoming velocity at half-height of the cylinders. Dashed lines show the extents of FOV 1, 2 and 3. Black rectangles illustrate the cylinder array of height h mounted on a circular patch. The origin $x = 0$ is at the centre of the patch and $y = 0$ is on the floor of the tunnel. Measurement data are not available in the hatched regions (between the cylinders). In panel (b), the blue arrow shows the location of the scalar point source.*

PIV measurements (Lee, Kevin, Monty, & Hutchins, 2016), $\Delta x^+ \times \Delta y^+ = 15 \times 15$ in streamwise and wall-normal directions, respectively.

2.3. Particle image velocimetry (PIV) and planar laser-induced fluorescence (PLIF)

For simultaneous planar PIV and PLIF measurements, the measurement domain is located in the streamwise–wall-normal (x–y) plane, slicing the centreline of the circular patch (figure 3). The measurement domain is created by combining three successive experiments in field of view (FOV) 1, FOV 2 and FOV 3, which extends downstream of the circular patch. Dashed lines in figure 3 illustrate these FOVs and the overlaps between each FOV. It should be noted that although the PIV and PLIF measurements are conducted simultaneously in each FOV, these measurements are not conducted simultanenously between FOV 1, 2 and 3. The PIV and PLIF images are recorded first in FOV 1, then the cameras and optics are traversed downstream to form FOV 2, then FOV 3. Each FOV has the size of 253 mm × 126 mm($x \times y$), which approximately extends 2.5 times the patch diameter ($2.5D$) in streamwise and $4h$ in height. When the three FOVs are stitched together, the total length in x is 689 mm ($6.89D$). Measurements are conducted in all three FOVs for the cylindrical array cases (C39, C64 and C133), and only the first two FOVs for solid obstruction and the reference TBL cases (CS and TBL, see table 1).

In each FOV, two 12-bit 4 MP CMOS cameras acquire the PIV images, while PLIF images are recorded by a 5.5 MP 16-bit sCMOS camera, to maximise the signal-to-noise ratio of the PLIF images. The PIV cameras are equipped with wavelength filters to filter out the PLIF signal, and vice versa for the PLIF camera. For PLIF measurements, a point source is created upstream of the circular patch by injecting Rhodamine 6G dye solution to the flow at a constant rate. The dye has the Schmidt number ($Sc \equiv \nu/\mathfrak{D}$, $\mathfrak{D}$ is the mass diffusivity) of 2500 ± 300 (Vanderwel & Tavoularis, 2014), which corresponds to the Peclet number based on patch diameter $Pe_D \equiv Re_D Sc = 1.12 \times 10^8$. The dye is supplied by a thin tube embedded on the floor of the tunnel, located 125 mm upstream from the centre the patch

https://doi.org/10.1017/flo.2022.2 Published online by Cambridge University Press

($x/D = 1.25$, see figure 3*b*). Scalar concentration fields presented in this study are normalised by the measured concentration at the point source, C_s. The complete description of the experimental set-up is given in appendix A. Further details on the PIV-PLIF measurements, calibration, post-processing and uncertainty analysis are given by Lim et al. (2021).

3. Results and discussions

3.1. Extent of the wake and scalar concentration

Figure 4(*a–d*) shows the contours of time-averaged streamwise velocity U for all porous test cases and the solid case (CS). The contours are normalised by $U_{h/2}$, which is defined as the incoming, undisturbed streamwise velocity upstream of the patch ($x/D = -1.3$) at the half-height of the cylinder, $y/h = 0.5$. The figures show the formation of wake for all porous and solid cases in the form of velocity deficit downstream of the patches. The magnitude of the deficit is significant, which signals the presence of patch-sized flow phenomena (Taddei et al., 2016) as opposed to those of individual cylinders observed in patches with low solidity (Chang & Constantinescu, 2015; Chen et al., 2012; Nicolai et al., 2020; Taddei et al., 2016). In figure 4(*b*,*c*), the blue-shaded contours show $U < 0$, which correspond to the recirculation of the flow downstream of the patch. The streamwise extent of the flow recirculation is approximately equal to D (figure 4*b*,*c*). The strength of the recirculating flow appears to be affected by the solidity of the patch: recirculation is not apparent in case C39 (case with the lowest solidity, figure 4*a*), a weak recirculation then appears in case C64 (figure 4*b*), which grows stronger in case C133 (figure 4*c*). It is also noted that the recirculation bubbles are shifted downstream as solidity decreases. In case C64 (figure 4*b*), the bubble is observed at $1 \lesssim x/D \lesssim 2$, while in case C133 (figure 4*c*) and the solid case CS (figure 4*d*), the bubbles form immediately at the trailing edge of the patches ($x/D = 0.5$). Similar phenomena have been observed in 2-D patches (Chang & Constantinescu, 2015), 3-D patches (Taddei et al., 2016; Zhou & Venayagamoorthy, 2019) and porous plates (Castro, 1971).

Superimposed with the contours of U in figure 4(*a–d*) are the contours of time-averaged spanwise vorticity $\Omega_y \equiv \partial V/\partial x - \partial U/\partial y$ normalised by $U_{h/2}/D$. Black solid lines are the contours of $\Omega_y < 0$ (clockwise) and the blue lines $\Omega_y > 0$ (counter-clockwise). Negative Ω_y show the development of shear layers forming above and downstream of the patches, which appear to be stronger (higher in magnitude) as solidity increases. The choice of using Ω_y is based on the inclusion of both $\mathrm{d}U/\mathrm{d}y$ and $\mathrm{d}V/\mathrm{d}x$, which is especially important when the vertical bleeding becomes significant (closer to leading edge of the patch at high solidities). Previous work (figure 10*a* in Nicolai et al., 2020) has shown that the vorticity and the Reynolds shear stress have similar behaviour. Similar to the observation by Taddei et al. (2016), here we also observe the elevation of the shear layer further upward from the patches as solidity increases (compare, for example, figure 4*c* with figure4*a*,*b*). The lift-off is attributed to vertical bleeding from the interior of the patches, which is noticeably absent in the solid case CS (figure 4*d*) where there is no vertical bleeding.

Figure 5(*a–d*) shows the contours of time-averaged scalar concentration C (normalised by the concentration at the source C_s and presented in logarithmic scale) for all porous test cases and the solid case. The dark-shaded contours in figure 5(*a–c*) illustrate how the scalar permeates through and downstream of the patches. With less obstructions to block the flow, high scalar concentration (purple-shaded contours) is observed downstream of the C39 and C64 patches in figure 5(*a*,*b*), respectively. As blockage (ϕ) increases, TE bleeding decreases and consequently, the downstream concentration decays (see C133 patch, figure 5*c*). Instead, the scalar escapes the patch by means of vertical bleeding, as shown by higher scalar concentration above the patch ($y/h \geq 1$) in figure 5(*c*). As ϕ reaches 1 (solid case), TE and vertical bleeding are non-existent, as evidenced by $C \approx 0$ above the patch and low magnitude of C downstream of the patch (figure 5*d*). Here, the observed concentration is mainly the result of flow mixing in the wake instead of the scalar permeating through the patch.

Figures 4 and 5 show the dependency of wake and scalar concentration downstream of the porous bodies as a result of TE bleeding. We attempt to measure the extent of the wake by using a similar

https://doi.org/10.1017/flo.2022.2 Published online by Cambridge University Press

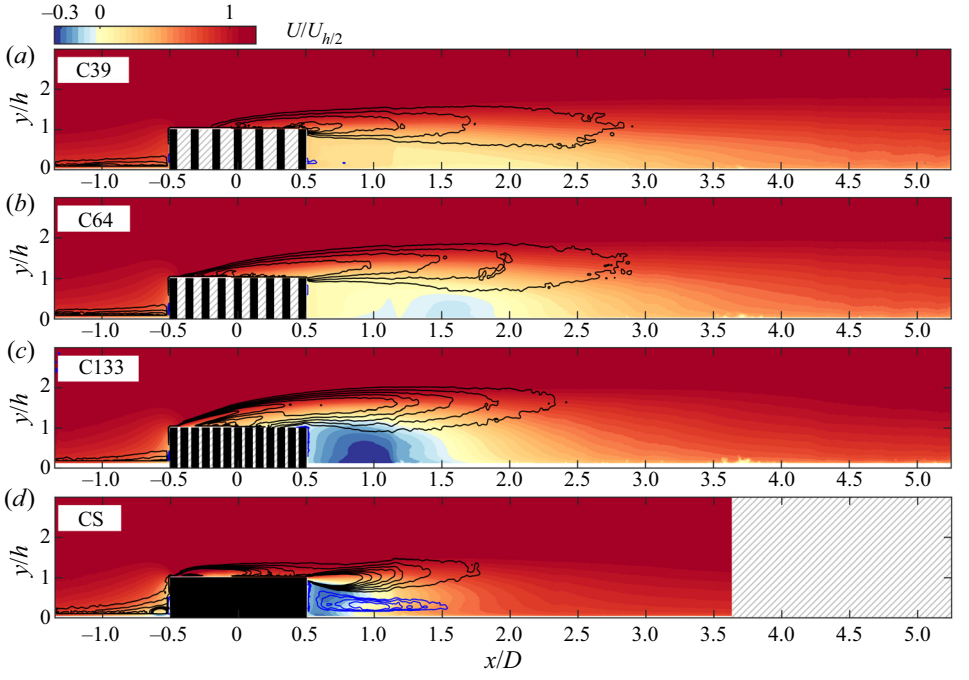

Figure 4. *Contours of time-averaged streamwise velocity $U/U_{h/2}$ of cases: (a) C39; (b) C64; (c) C133 and (d) CS. Lines are the time-averaged spanwise vorticity $\Omega_y D/U_{h/2}$ with the contour levels of* $-8, -7, \ldots, -2$ *(solid line) and* $0.4, 0.8, \ldots, 1.6$ *(solid blue line).*

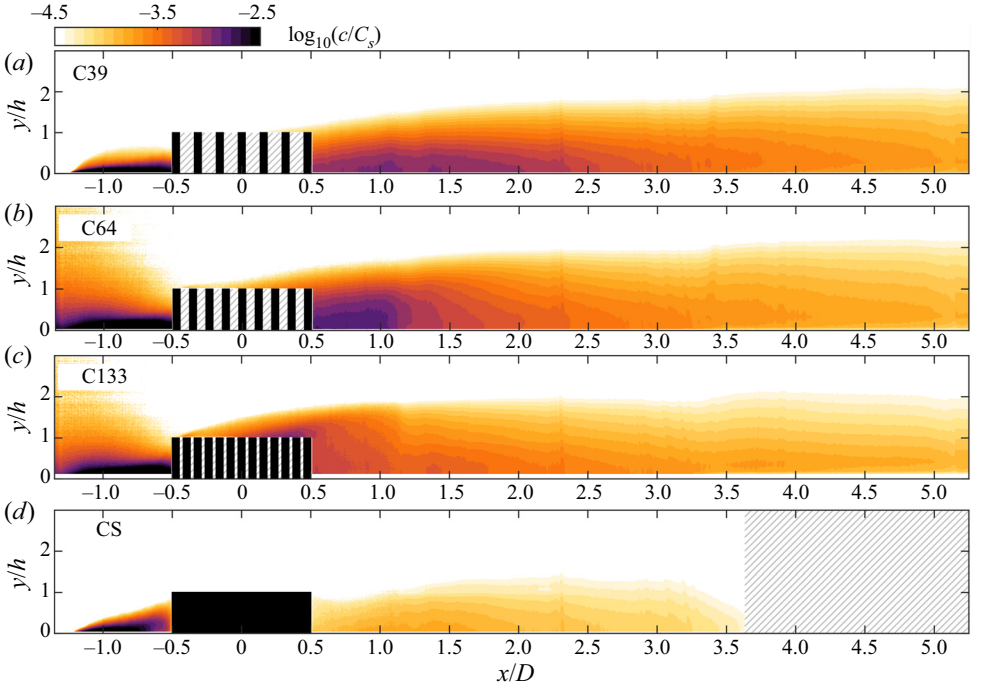

Figure 5. *Contours of time-averaged scalar concentration C/C_s (in logarithmic scale) of cases: (a) C39; (b) C64; (c) C133 and (d) CS. Measurement data are not available in the hatched regions.*

https://doi.org/10.1017/flo.2022.2 Published online by Cambridge University Press

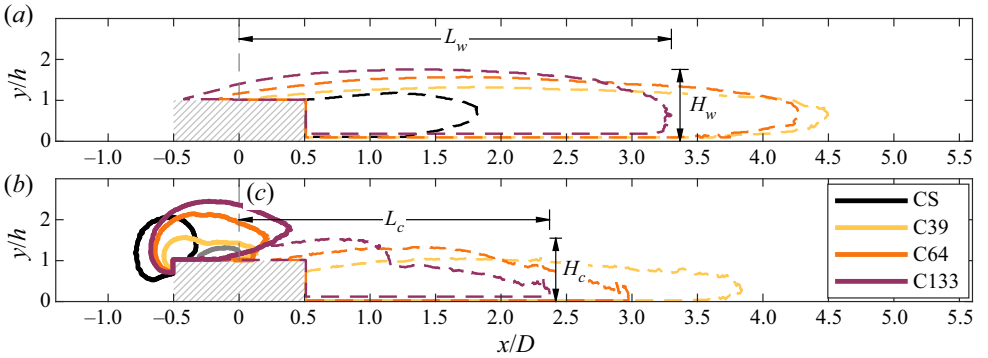

Figure 6. *Contours of time-averaged (a) defect velocity $\Delta U/U_{h/2} = 0.3$, (b) wall-normal velocity $V/U_{h/2} = 0.1$ at $x/D \leq 0.5$ and (c) scalar concentration $C/C_s = 3 \times 10^{-4}$. Legends in panel (b) show the colour scheme for each case. Hatched regions illustrate the location of the patch. In panels (a,c), the horizontal and vertical extent of the wake are defined by L_w and H_w, respectively, while L_c and H_c are the horizontal and vertical extent of the scalar dispersion. In panel (b), the grey solid line is the wall-normal velocity ($V/U_{h/2} = -0.07$) of case CS.*

method to Nicolai et al. (2020). First, we define the velocity defect as $\Delta U = U_{bl} - U$, where $U_{bl}(y)$ is the incoming boundary layer velocity profile upstream of the patch (at $x/D = -1.3$), and arbitrarily choose a threshold for the magnitude of ΔU as a wake definition. Figure 6(*a*) shows the contours of $\Delta U/U_{h/2}$ for all porous cases and the solid case at the chosen threshold of 0.3. With this threshold, we are able to define the length and height of the wake, L_w and H_w, respectively (figure 6*a*). Here, L_w is defined as the length of the wake measured from the centreline of the patch ($x = 0$) to the x-maxima of the chosen contour level, while H_w is the height of the wake measured from the floor of the tunnel ($y = 0$) to the y-maxima of the same contour level. Figure 7(*a*,*b*) shows the normalised length and height of the wake, L_w/D and H_w/h, respectively, as a function of solidity ϕ. The figures show that L_w decreases with increasing ϕ, but H_w increases (and possibly reaches a maxima at a certain value of ϕ) and then decreases as $\phi \rightarrow 1$, where the obstacle is no longer porous and there is no flow escaping from the top of the patch. The wake 'blow-up' (i.e. taller wake) in higher ϕ has also been recorded by Taddei et al. (2016) and Nicolai et al. (2020). These tendencies of L_w and H_w are insensitive to the change in threshold, as illustrated by the hatched regions in figure 7(*a*,*b*), which correspond to the same quantities measured when the threshold for $\Delta U/U_{h/2}$ is varied by $0.3 \pm 20\,\%$. As a comparison, L_w and H_w measured by Nicolai et al. (2020) are shown in white-filled circles in figure 7(*a*,*b*). The study involved similar arrays of cylindrical patches of various $\phi (0.018 \leq \phi \leq 1)$ that impinged a developing turbulent boundary layer at $Re_\theta \approx 60\,000$ (20 times higher than that of the current study). It should be noted that the measured L_w and H_w are greater in magnitude as the wake is defined at a lower threshold of $\Delta U/U_{h/2} = 0.2$ instead of 0.3 due to the increasing streamwise length of the FOV ($8D$ instead of $6.89D$). It should also be noted that the values of H_w (white-filled circles in figure 7*b*) are scaled by a factor of $3.58h/\delta_{bl}$, where 3.58 is the ratio of incoming boundary layer thickness to cylinder height δ_{bl}/h of Nicolai et al. (2020). However, the differences between studies do not change the observed trend in L_w and H_w as a function of ϕ.

Similarly, a threshold can also be applied to the scalar concentration field C to measure the extent of scalar dispersion downstream of the patch. Figure 6(*c*) shows the contours of C/C_s for all porous cases and the solid case at the chosen threshold of 3×10^{-4}. The length and height of scalar dispersion L_c and H_c, respectively, are measured from the centreline of the patch $x = 0$ to the x-maxima of the chosen contour level and from the floor of the tunnel $y = 0$ to the y-maxima, respectively. Filled diamonds in figure 7(*a*,*b*) show the measured L_c and H_c as a function of ϕ. Similar to those of the wake extent, L_c and H_c decreases and increases, respectively, with increasing ϕ. It should be noted that although scalar

https://doi.org/10.1017/flo.2022.2 Published online by Cambridge University Press

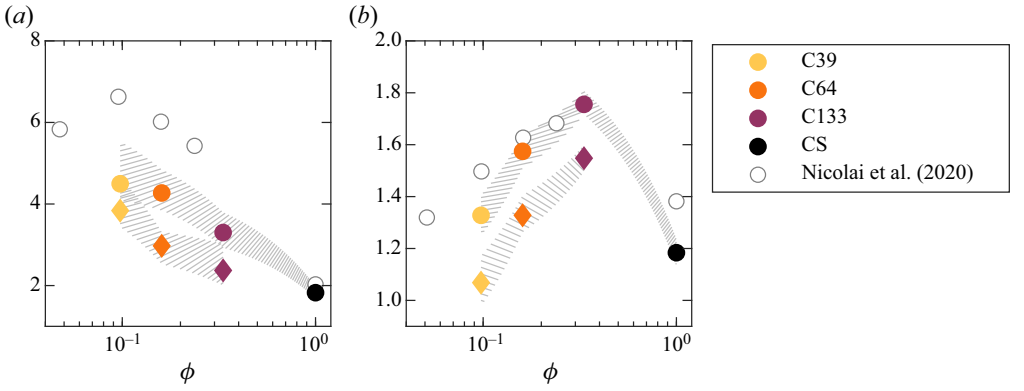

Figure 7. *(a) Normalised length of wake L_w/D (•) and scalar dispersion L_c/D (♦) (as illustrated in figure 6) of all test cases as a function of solidity ϕ. (b) Height of wake H_w/h (•) and scalar dispersion H_c/h (♦). Hatched regions illustrate the sensitivity to the threshold level defining the length/height (±20 %). The same quantities measured by Nicolai et al. (2020) at $Re_\theta \approx 60\,000$ are shown for comparison. Legends show the colour scheme for each case.*

concentration data are available for case CS, the magnitude of C downstream of the patch is lower than that of the chosen threshold (see figure 5*d*) and thus we are unable to measure L_c and H_c for this case.

Figure 8(*a–d*) shows the coloured contours of C at the trailing edge for all porous and solid cases, with black contour lines superimposed in the figures showing $U < 0$, corresponding to flow recirculation. For case C64, figure 8(*b*) shows a high scalar concentration (purple-shaded region) at the trailing edge and up to $x/D \approx 1$, immediately followed by the emergence of a recirculation bubble. In other words, the scalar is trapped between the porous patch upstream and the recirculation bubble that prevents the scalar from convecting downstream. By contrast, case C39 (figure 8*a*) that has lower solidity shows no recirculation bubble, and thus the scalar is freely transported downstream of the patch. Case C133 (figure 8*c*), however, shows the recirculation bubble being shifted to the trailing edge. The scalar in this case is largely prevented from escaping towards the trailing edge (this explains the decrease in L_w and L_c as solidity increases, see figure 7*a*). Conservation laws dictate two possible outlets left for the flow: lateral and vertical bleeding. The higher magnitude of C above the patch, upstream of the bubble ($y/h \geq 1$, $0 \leq x/D \leq 0.5$) confirms increasing vertical bleeding in higher solidity, while the increase of lateral bleeding with ϕ has been confirmed by Zhou and Venayagamoorthy (2019). In some sense, the flow lingers downstream of the porous obstruction (characterised by high magnitude of C in this region in case C64), it is as if the obstruction is 'extended' in the streamwise direction. The length of this extension seems to be inversely proportional to ϕ, as it is longer than the FOV for case C39 (or perhaps infinitely long), approximately equal to $1.25D$ for case C64 (figure 8*b*) and 0 for case C133 (figure 8*c*). Possibly, the extension length is akin to the length of the steady wake region observed in 2-D patches (Ball et al., 1996; Chen et al., 2012; Zong & Nepf, 2012). When the obstruction is impermeable (figure 8*d*), the mechanism differs. It acts as a solid body, shedding a pair of shear layers at the trailing edge (see contours of Ω_y at $0.5 \leq x/D \leq 1.5$ in figure 4*d*).

Figure 8(*a–c*) shows the contours of $\Omega_y < 0$ as solid grey lines, representing the shear layer forming above the porous patches. In case C39 (figure 8*a*), the shear layer shields a region of (relatively) high scalar concentration (coloured contours in figure 8*a*) below the layer. As solidity increases in case C64 (figure 8*b*), higher C is observed downstream of the patch (purple-shaded contours), which coincides with elevation of the shear layer compared with that of C39 in figure 8(*a*). In the case with the highest solidity (C133 in figure 8*c*), recirculation occurs on the trailing edge followed by higher C above the patch compared with that downstream of the patch. Here the shear layer is elevated further upward, shielding the observed high C above the patch ($0.25 \lesssim x/D \lesssim 0.5$). Here, there seems to be an 'artificial'

https://doi.org/10.1017/flo.2022.2 Published online by Cambridge University Press

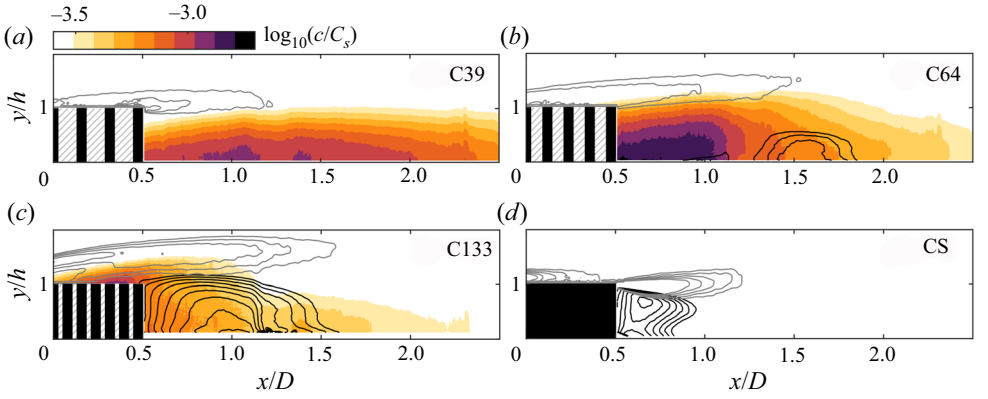

Figure 8. *Contours of scalar concentration* $\log_{10}(C/C_s)$ *for cases: (a) C39; (b) C64; (c) C133 and (d) CS. Black solid lines are negative streamwise velocity, in panel (b)* $U/U_{h/2} = -0.06, -0.04, -0.02$ *and in panels (c,d)* $-0.4, -0.36, \ldots -0.04$. *Gray solid lines are the normalised vorticity in y axis* $\Omega_y D/U_{h/2} = -8, -7, \ldots, -4$.

upward extension of the porous obstruction as ϕ increases, which accompanies the previously discussed streamwise extension at the TE of the obstruction.

3.2. Trailing edge and vertical bleeding

We further quantify the velocity of TE bleeding U_{bleed}. Here, U_{bleed} is defined as U downstream of the patch ($x \geq D/2$) integrated over y. This definition can be extended further to the scalar concentration at the trailing edge C_{te}, such that

$$U_{bleed}(x) = \frac{1}{h}\int_0^h U(x,y)\,\mathrm{d}y; \quad C_{te}(x) = \frac{1}{h}\int_0^h C(x,y)\,\mathrm{d}y \quad \text{for } x \geq D/2. \tag{3.1a,b}$$

Figure 9(*a*) shows the magnitude of U_{bleed} at the trailing edge, $x = D/2$, as a function of ϕ. White-filled circles are U_{bleed} measured by Nicolai et al. (2020) for similar cylindrical arrangements at $Re_\theta \approx 60\,000$. Despite the difference in the order of Re, both Nicolai et al. (2020) and the present study show that U_{bleed} decreases with ϕ at the trailing edge. Figure 9(*b*,*c*) further shows the defects $1 - U_{bleed}/U_{h/2}$ and C_{te}/C_s as functions of x downstream of the patch ($x \geq D/2$). Both figures show the decay of wake and scalar concentration with x, with (generally) faster decay as ϕ increases in the porous cases. In particular, U_{bleed} in figure 9(*b*) shows that the solid case CS recovers the fastest to the upstream condition (i.e. the incoming flow, dashed line is the smooth-wall case TBL), followed by the highest solidity case C133. We note that the decay of the wake for the porous and solid cases (figure 9*b*) and the decay of C for the porous cases (figure 9*c*) seem to follow a certain power law, possibly similar to that of Wygnanski, Champagne, and Marasli (1986) for various solid and porous wake generators, which is left for future works. The exception to this is the scalar concentration downstream of case CS (black solid line in figure 9*c*), which is approximately constant in x and much lower in magnitude compared with the porous cases.

A closer look into figure 9(*c*) reveals that the integrated scalar concentration of case C64 peaks at $x/D \approx 1$, and the magnitude of this peak is much higher than that of cases with lower and higher ϕ (C39 and C133). This spike corresponds to the high scalar concentration (purple-shaded region) at the trailing edge and up to $x/D \approx 1$, which is immediately followed by the emergence of a recirculation bubble (figure 8*b*) and thus can be translated into the streamwise extension of the porous obstruction discussed in § 3.1.

https://doi.org/10.1017/flo.2022.2 Published online by Cambridge University Press

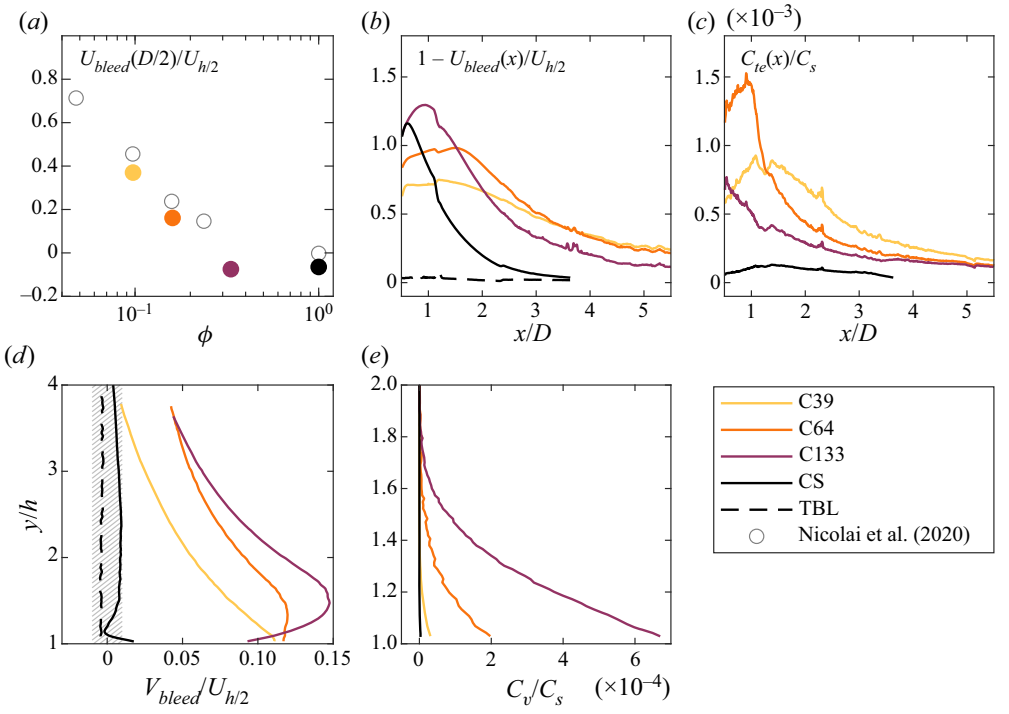

Figure 9. *(a) Integrated velocity bleeding $U_{bleed}/U_{h/2}$ at the trailing edge $x = D/2$. The same quantity measured by Nicolai et al. (2020) is shown for comparison. (b) $1 - (U_{bleed}/U_{h/2})$ as a function of x downstream of the patch. (c) Integrated scalar concentration C_{te}/C_s as a function of x. (d) Integrated vertical bleeding $V_{bleed}/U_{h/2}$ above the patch ($y/h > 1$) as a function of y. (e) Integrated scalar concentration above the patch C_v/C_s. In panels (b,d), the dashed line is the reference smooth-wall case TBL. In panel (d), hatched region shows $V_{bleed} \pm 1$ % of $U_{h/2}$. Legends show the colour scheme for each case.*

Contours of positive (upward) wall-normal velocity $V > 0$ above the patches are shown in solid lines in figure 6(*b*) for the same magnitude $V/U_{h/2} = 0.1$. The contours reveal a very different pattern of flow above the patches for porous cases compared with the solid case CS (solid black line). In case CS, flow separation is characterised by high magnitude of V observed in the leading edge of the patch ($x/D = -0.5$). Compared with the solid case, the magnitude of V in the leading edge is lower for all porous cases, as the flow is able to penetrate the patches instead of being diverted upward (see Taddei et al. (2016) for similar 3-D patches and Zhou and Venayagamoorthy (2019) for suspended patches, note that the sign of V is inverted in the latter). What is only observed in the porous patches, however, is the presence of vertical bleeding above the patches, characterised by the contours of $V > 0$ at $-0.5 \leq x/D \leq 0.5$ and $y/h \geq 1$. The magnitude and extent of this region appear to be dependent upon solidity. For the same magnitude of $V/U_{h/2}$, the contours for porous cases in figure 6(*b*) show that V is extended upward (in y) as ϕ increases.

Similar to the analysis for the TE bleeding U_{bleed}, we quantify the magnitude of vertical bleeding as the integrated V above the patch ($-D/2 \leq x \leq D/2$ and $y \geq h$), and this can be further extended to include the scalar concentration,

$$V_{bleed}(y) = \frac{1}{D}\int_{-D/2}^{D/2} U(x,y)\,\mathrm{d}x; \quad C_v(y) = \frac{1}{D}\int_{-D/2}^{D/2} C(x,y)\,\mathrm{d}x \quad \text{for } y \geq h. \tag{3.2a,b}$$

https://doi.org/10.1017/flo.2022.2 Published online by Cambridge University Press

Figure 9(*d*,*e*) shows the integrated vertical bleeding V_{bleed} and scalar concentration C_v as functions of y above the patch. Both figures show higher magnitude of V_{bleed} and C_v closer to the patch, which decay further towards the free stream. Dependency on ϕ is apparent on both. In figure 9(*d*), V_{bleed} generally increases with ϕ, with a significantly smaller magnitude (within ±1 % of the incoming flow $U_{h/2}$, see hatched region in figure 9*d*) for CS and TBL (black solid and dashed lines in figure 9*d*, respectively). For case CS, small V_{bleed} is the result of averaging between $V > 0$ in the leading edge and $V < 0$ above the patch (see black and grey contour lines in figure 6*b*), while for case TBL ($V = 0$), this can be attributed to the error of the measurements. The integrated scalar concentration in figure 9(*e*) is 0 for the solid case CS (since there is no vertical bleeding, see black solid line in figure 9*e*), while for the porous cases, it increases with ϕ and decays to 0 further from the patch.

In addition to increasing vertical bleeding with ϕ, we also observed that the maxima of C_v in figure 9(*e*) occurs at the top surface of the patch $y/h = 1$ for all porous cases, but the maxima of V_{bleed} in figure 9(*d*) occurs further from the patch (for example, it occurs at $y/h \approx 1.5$ for case C133 in figure 9*d*). This perhaps can be explained by the upward extension of the porous patches (figure 8*c*). Here, the high scalar concentration (purple-shaded contours in figure 8*c*) occurs exactly at the top surface of the patch (corresponding to maximum C_v) and the porous obstruction is artificially extended upward (corresponding to the maximum V_{bleed} further from the top surface).

4. Conclusions and recommendations

We conducted planar PIV-PLIF measurements of the flow surrounding 3-D, circular porous patches of various solidity $\phi(0.098 \leq \phi \leq 1)$ to study the characteristics of flow in the wake of and above the patches. Porosity is generated by mounting rigid cylinders of height h and diameter d on the patch (whose diameter is D) and the variation in ϕ is achieved by systematically increasing the number of cylinders in a patch. The patches are fully submerged within the incoming flow, with a fluorescent dye injected from the floor of the tunnel, creating a point source upstream of the patches. Simultaneous PIV-PLIF measurements in the x–y plane provide streamwise and wall-normal velocity components, as well as the concentration of the fluorescent tracer in the FOV.

Examination of the time-averaged velocity and scalar fields suggests that the trailing edge (longitudinal) and vertical flow bleeding from the obstructions decreases and increases with increasing ϕ, respectively, as previously reported by Taddei et al. (2016), Zhou and Venayagamoorthy (2019), Nicolai et al. (2020). In addition to that, we observe that ϕ affects the scalar concentration in the wake and above the patch. In particular, the present results suggest that ϕ determines the following components.

(i) The horizontal extent of the wake (L_w) and scalar concentration (L_c) downstream of the porous patches, with L_w and L_c decreasing with ϕ (figure 7*a*). The decrease is attributed to the shift of recirculation bubbles towards the trailing edge of the patches as ϕ increases. High scalar concentration is observed downstream of the patch as the flow is trapped between patches and the recirculation bubble, acting as an elongation of the obstructions in streamwise direction.

(ii) The vertical extent of the wake (H_w) and scalar concentration (H_c) downstream of the porous patches, with H_w and H_c increasing with ϕ (figure 7*b*). As ϕ increases further, a recirculation bubble occurs at the trailing edge of the patch and the flow is trapped in the interior of the patch. The flow largely escapes by means of vertical (and lateral) bleeding. High concentration of scalar, elevation of shear layer and V above the patch suggest that the flow is trapped between the top surface of the patch, from which the flow bleeds, and the shear layer. Here we observe an artificial extension of the obstacle further upward (i.e. the patch is 'taller' from the perspective of the flow) as ϕ increases.

As a final remark, theauthors would like to note that this study is the first step towards understanding both momentum and scalar transport of the flow surrounding 3-D porous obstructions and building useful models for engineering design, prediction for meteorological or oceanographic flows, etc. The results presented in this study are limited to the time-averaged velocity and scalar components. However,

https://doi.org/10.1017/flo.2022.2 Published online by Cambridge University Press

Table 2. *Dye concentration for each FOV: C_1 and C_2 are the concentration of dye inside the two tanks used to obtain calibration coefficients A_{cal}. Here, C_s is the concentration of dye at the point source during experiments (figure 3b).*

FOV	C_1 [mg L^{-1}]	C_2 [mg L^{-1}]	C_s [mg L^{-1}]
1	0.10	0.3	0.3
2	0.05	0.1	10
3	0.05	0.1	10

we note that intermittency (i.e. discrepancies between the time-averaged and instantaneous flow fields) has been reported by Cassiani, Katul, and Albertson (2008) and Taddei et al. (2016). In the future, analysis about the fluctuating components (u', v' and c') should be included to obtain the full picture of the flow characteristics. The decay of wake and scalar concentration in the trailing edge, shown in figure 7(*d*,*e*), indicate a possible wake model for both porous and solid cases, which should also be investigated in the future.

Declaration of Interests. The authors report no conflict of interest.

Funding Statement. The authors gratefully acknowledge the financial support from EPSRC (grant nos. EP/P021476/1 and EP/S013296/1).

Author Contributions. C.N. designed, performed all measurements, and processed the data. D.D.W. processed, analysed the data and wrote the manuscript, with supervision from B.G.

Data Availability Statement. Data published in this article are available on the University of Southampton repository https://doi.org/10.5258/SOTON/D2137.

Ethical Standards. The research meets all ethical guidelines, including adherence to the legal requirements of the study country.

Appendix A. Details of simultaneous PIV-PLIF measurements and data processing

The circular patches and cylinders are made of photopolymer resin (Young's modulus $E = 2.7$ GPa) and manufactured using a Form 2 3-D printer (Formlabs Inc). These patches are mounted at the centreline of the tunnel (maximum spanwise distance from the side walls) and illuminated by Nano-PIV L50-100 Nd:YAG 100 mJ double-pulsed laser (532 nm emission wavelength) in the x–y plane for PIV-PLIF measurements. The flow is seeded with polyamide particles (diameter 50 μm). As many as 3000 image pairs are acquired by two PIV cameras for each case at the rate of 4 Hz, which corresponds to the boundary-layer turnover rate of $TU_\infty/\delta_{bl} = 1.4$. The timing between a pair of PIV images is ∼1 ms ($t^+ \equiv \Delta t U_{\tau bl}^2/\nu \approx 0.32$). Image cross-correlation and post-processing of the resulting velocity vectors are conducted using a commercial software (DaVis, LaVision GmbH), with the final window size of 24×24 pixels (75 % overlap) and image pixel size of 15 pixels/mm, which corresponds to the spatial resolution of $\Delta x^+ \times \Delta y^+ = 15 \times 15$ for case TBL.

For PLIF measurements, the dye (Rhodamine 6G) is supplied by gravity through a thin tube (diameter 3 mm) embedded at the floor of the tunnel at a 45° angle. A needle valve releases the dye to the flow at a constant rate of 30 cc min^{-1}. The absorption and emission peaks of Rhodamine 6G are at 525 and 554 nm, respectively. Thus, to block out all light (including that reflected from PIV particles) except the PLIF signal, a longpass filter with 540 nm cutoff is installed in front of the PLIF camera. To reduce the uncertainty of the scalar concentration measurements, the laser power (E_{ref}) is recorded at each pulse by an in-line power energy monitor. To maximise the signal-to-noise ratio of the scalar concentration, the dye concentration C_s is varied based on the location of the FOV relative to the point source (table 2). The instantaneous scalar concentration field c is obtained using the relation $c = A_{cal}(I/E_{ref} - I_0)$, where I is the intensity of the PLIF image and I_0 is the intensity of the background image (without dye, $C_0 = 0$ mg L^{-1}), normalised by E_{ref} recorded during calibration. Here, A_{cal} is the PLIF calibration

https://doi.org/10.1017/flo.2022.2 Published online by Cambridge University Press

coefficient, obtained by capturing an image of a small tank filled with the dye of known concentration. Two tanks with different dye concentrations (C_1 and C_2) are used for calibration (table 2). The final calibration coefficient A_{cal} is obtained by averaging the coefficients calculated from C_1 and C_2, $A_{cal} = (A_1 + A_2)/2$. Further details of the calibration technique and image correction are given by Vanderwel and Tavoularis (2014) and Lim et al. (2021).

Geometrical masking is performed on both PIV and PLIF images to remove the cylinders that block the cameras' view and laser reflections around the edge of the cylinders. Due to masking, measurement data are not available in the region inside the canopy (between the cylinders, see figure 3). It should be noted that the spatial resolution of the resulting PIV vector fields is lower than that of the scalar concentration fields from PLIF due to the use of an interrogation window during cross-correlation. The scalar field presented in this study is downsampled and mapped to the vector field coordinate system with 2-D linear interpolation.

References

Ahmadian, R., Falconer, R., & Bockelmann-Evans, B. (2012). Far-field modelling of the hydro-environmental impact of tidal stream turbines. *Renewable Energy*, *38*(1), 107–116. https://doi.org/10.1016/j.renene.2011.07.005.

Aristodemou, E., Boganegra, L. M., Mottet, L., Pavlidis, D., Constantinou, A., Pain, C., Robins, A., & ApSimon, H. (2018). How tall buildings affect turbulent air flows and dispersion of pollution within a neighbourhood. *Environmental Pollution*, *233*, 782–796. https://doi.org/10.1016/j.envpol.2017.10.041.

Baidya Roy, S., Pacala, S. W., & Walko, R. (2004). Can large wind farms affect local meteorology? *Journal of Geophysical Research: Atmospheres*, *109*, D19101. https://doi.org/10.1029/2004JD004763.

Ball, D., Stansby, P., & Allison, N. (1996). Modelling shallow water flow around pile groups. *Proceedings of the Institution of Civil Engineers Water Maritime & Energy*, *118*(4), 226–236.

Cassiani, M., Katul, G., & Albertson, J. (2008). The effects of canopy leaf area index on airflow across forest edges: Large-eddy simulation and analytical results. *Boundary-Layer Meteorology*, *126*(3), 433–460. https://doi.org/10.1007/s10546-007-9242-1.

Castro, I. (1971). Wake characteristics of two-dimensional perforated plates normal to an air-stream. *Journal of Fluid Mechanics*, *46*(3), 599–609. https://doi.org/10.1017/S0022112071000727.

Chang, K., & Constantinescu, G. (2015). Numerical investigation of flow and turbulence structure through and around a circular array of rigid cylinders. *Journal of Fluid Mechanics*, *776*, 161–199. https://doi.org/10.1017/jfm.2015.321.

Chang, W.-Y., Constantinescu, G., & Tsai, W. F. (2017). On the flow and coherent structures generated by a circular array of rigid emerged cylinders placed in an open channel with flat and deformed bed. *Journal of Fluid Mechanics*, *831*, 1–40. https://doi.org/10.1017/jfm.2017.558.

Chen, Z., Jiang, C., & Nepf, H. (2013). Flow adjustment at the leading edge of a submerged aquatic canopy. *Water Resources Research*, *49*(9), 5537–5551. https://doi.org/10.1002/wrcr.20403.

Chen, Z., Ortiz, A., Zong, L., & Nepf, H. (2012). The wake structure behind a porous obstruction and its implications for deposition near a finite patch of emergent vegetation. *Water Resources Research*, *48*(9), W09517. https://doi.org/10.1029/2012WR012224.

De Langre, E. (2008). Effects of wind on plants. *Annual Review of Fluid Mechanics*, *40*, 141–168. https://doi.org/10.1146/annurev.fluid.40.111406.102135.

Finnigan, J. (2000). Turbulence in plant canopies. *Annual Review of Fluid Mechanics*, *32*(1), 519–571. https://doi.org/10.1146/annurev.fluid.32.1.519.

Huang, J., Cassiani, M., & Albertson, J. (2009a). Analysis of coherent structures within the atmospheric boundary layer. *Boundary-Layer Meteorology*, *131*(2), 147–171. https://doi.org/10.1007/s10546-009-9357-7.

Huang, J., Cassiani, M., & Albertson, J. (2009b). The effects of vegetation density on coherent turbulent structures within the canopy sublayer: A large-eddy simulation study. *Boundary-Layer Meteorology*, *133*(2), 253–275. https://doi.org/10.1007/s10546-009-9423-1.

Huang, J., Cassiani, M., & Albertson, J. (2011). Coherent turbulent structures across a vegetation discontinuity. *Boundary-Layer Meteorology*, *140*(1), 1–22. https://doi.org/10.1007/s10546-011-9600-x.

Kanda, M. (2006). Large-eddy simulations on the effects of surface geometry of building arrays on turbulent organized structures. *Boundary-Layer Meteorology*, *118*(1), 151–168. https://doi.org/10.1007/s10546-005-5294-2.

Katul, G., Kuhn, G., Schieldge, J., & Hsieh, C.-I. (1997). The ejection-sweep character of scalar fluxes in the unstable surface layer. *Boundary-Layer Meteorology*, *83*(1), 1–26. https://doi.org/10.1023/A:1000293516830.

Kemp, J. L., Harper, D. M., & Crosa, G. A. (2000). The habitat-scale ecohydraulics of rivers. *Ecological Engineering*, *16*(1), 17–29. https://doi.org/10.1016/S0925-8574(00)00073-2.

Lee, J., Kevin, , Monty, J., & Hutchins, N. (2016). Validating under-resolved turbulence intensities for PIV experiments in canonical wall-bounded turbulence. *Experiments in Fluids*, *57*, 129. https://doi.org/10.1007/s00348-016-2209-6.

Lei, J., & Nepf, H. (2021). Evolution of flow velocity from the leading edge of 2-D and 3-D submerged canopies. *Journal of Fluid Mechanics*, *916*, 0–0. https://doi.org/10.1017/jfm.2021.197.

https://doi.org/10.1017/flo.2022.2 Published online by Cambridge University Press

Li, D., & Bou-Zeid, E. (2011). Coherent structures and the dissimilarity of turbulent transport of momentum and scalars in the unstable atmospheric surface layer. *Boundary-Layer Meteorology*, *140*(2), 243–262. https://doi.org/10.1007/s10546-011-9613-5.

Lim, H. D., Hertwig, D., Grylls, T., Gough, H., van Reeuwijk, M., Grimmond, S., & Vanderwel, C. (2021). Pollutant dispersion by tall buildings: Laboratory experiments and Large-Eddy Simulation. *Experiments in Fluids*, EXIF-D-21-00325 (submitted).

Myers, L., & Bahaj, A. (2012). An experimental investigation simulating flow effects in first generation marine current energy converter arrays. *Renewable Energy*, *37*(1), 28–36. https://doi.org/10.1016/j.renene.2011.03.043.

Nepf, H. M. (1999). Drag, turbulence, and diffusion in flow through emergent vegetation. *Water Resources Research*, *35*(2), 479–489. https://doi.org/.org/10.1029/1998WR900069.

Nepf, H. M. (2012a). Flow and transport in regions with aquatic vegetation. *Annual Review of Fluid Mechanics*, *44*, 123–142. https://doi.org/10.1146/annurev-fluid-120710-101048.

Nepf, H. M. (2012b). Hydrodynamics of vegetated channels. *Journal of Hydraulic Research*, *50*(3), 262–279. https://doi.org/10.1080/00221686.2012.696559.

Nepf, H., Mugnier, C., & Zavistoski, R. (1997). The effects of vegetation on longitudinal dispersion. *Estuarine, Coastal and Shelf Science*, *44*(6), 675–684. https://doi.org/10.1006/ecss.1996.0169.

Nicolai, C., Taddei, S., Manes, C., & Ganapathisubramani, B. (2020). Wakes of wall-bounded turbulent flows past patches of circular cylinders. *Journal of Fluid Mechanics*, *892*, A37. https://doi.org/10.1017/jfm.2020.102.

Nicolle, A., & Eames, I. (2011). Numerical study of flow through and around a circular array of cylinders. *Journal of Fluid Mechanics*, *679*, 1–31. https://doi.org/10.1017/jfm.2011.77.

Plew, D. R. (2011). Depth-averaged drag coefficient for modeling flow through suspended canopies. *Journal of Hydraulic Engineering*, *137*(2), 234–247. https://doi.org/10.1061/ASCEHY.1943-7900.0000300.

Poggi, D., Katul, G., & Albertson, J. (2006). Scalar dispersion within a model canopy: Measurements and three-dimensional lagrangian models. *Advances in Water Resources*, *29*(2), 326–335. https://doi.org/10.1016/j.advwatres.2004.12.017.

Poggi, D., Porporato, A., Ridolfi, L., Albertson, J., & Katul, G. (2004). The effect of vegetation density on canopy sub-layer turbulence. *Boundary-Layer Meteorology*, *111*(3), 565–587. https://doi.org/10.1023/B:BOUN.0000016576.05621.73.

Rajewski, D. A., Takle, E. S., Prueger, J. H., & Doorenbos, R. K. (2016). Toward understanding the physical link between turbines and microclimate impacts from in situ measurements in a large wind farm. *Journal of Geophysical Research: Atmospheres*, *121*(22), 13–392. https://doi.org/10.1002/2016JD025297.

Raupach, M., & Thom, A. (1981). Turbulence in and above plant canopies. *Annual Review of Fluid Mechanics*, *13*(1), 97–129. https://doi.org/10.1146/annurev.fl.13.010181.000525.

Rominger, J. T., & Nepf, H. M. (2011). Flow adjustment and interior flow associated with a rectangular porous obstruction. *Journal of Fluid Mechanics*, *680*, 636–659. https://doi.org/https://doi.org/10.1017/jfm.2011.199.

Schlichting, H., & Gersten, K. (2017). *Boundary-Layer Theory* (9th ed.). Heidelberg: Springer-Verlag Berlin. https://doi.org/10.1007/978-3-662-52919-5.

Sillero, J., Jiménez, J., & Moser, R. (2014). Two-point statistics for turbulent boundary layers and channels at Reynolds numbers up to $\delta^+ \approx 2000$. *Physics of Fluids*, *26*, 105109. https://doi.org/10.1063/1.4899259.

Taddei, S., Manes, C., & Ganapathisubramani, B. (2016). Characterisation of drag and wake properties of canopy patches immersed in turbulent boundary layers. *Journal of Fluid Mechanics*, *798*, 27–49. https://doi.org/10.1017/jfm.2016.312.

Tanino, Y., & Nepf, H. M. (2008). Lateral dispersion in random cylinder arrays at high Reynolds number. *Journal of Fluid Mechanics*, *600*, 339–371. https://doi.org/10.1017/S0022112008000505.

Tinoco, R. O., & Coco, G. (2016). A laboratory study on sediment resuspension within arrays of rigid cylinders. *Advances in Water Resources*, *92*, 1–9. https://doi.org/10.1016/j.advwatres.2016.04.003.

Tseung, H. L., Kikkert, G. A., & Plew, D. (2016). Hydrodynamics of suspended canopies with limited length and width. *Environmental Fluid Mechanics*, *16*(1), 145–166. https://doi.org/10.1007/s10652-015-9419-y.

Vanderwel, C., & Tavoularis, S. (2014). On the accuracy of PLIF measurements in slender plumes. *Experiments in Fluids*, *55*(8), 1–16. https://doi.org/10.1007/s00348-014-1801-x.

Vennell, R. (2011). Tuning tidal turbines in-concert to maximise farm efficiency. *Journal of Fluid Mechanics*, *671*, 587–604. https://doi.org/10.1017/S0022112010006191.

White, B. L., & Nepf, H. M. (2003). Scalar transport in random cylinder arrays at moderate Reynolds number. *Journal of Fluid Mechanics*, *487*, 43–79. https://doi.org/10.1017/S0022112003004579.

Wygnanski, I., Champagne, F., & Marasli, B. (1986). On the large-scale structures in two-dimensional, small-deficit, turbulent wakes. *Journal of Fluid Mechanics*, *168*, 31–71. https://doi.org/10.1017/S0022112086000289.

Zhou, J., & Venayagamoorthy, S. K. (2019). Near-field mean flow dynamics of a cylindrical canopy patch suspended in deep water. *Journal of Fluid Mechanics*, *858*, 634–655. https://doi.org/10.1017/jfm.2018.775.

Zong, L., & Nepf, H. (2012). Vortex development behind a finite porous obstruction in a channel. *Journal of Fluid Mechanics*, *691*, 368–391. https://doi.org/10.1017/jfm.2011.479.

Cite this article: D. D. Wangsawijaya, C. Nicolai and B. Ganapathisubramani (2022). Time-averaged velocity and scalar fields of the flow over and around a group of cylinders: a model experiment for canopy flows. *Flow*, *2*, E9. doi:10.1017/flo.2022.2